AGU PUBLICATIONS

Geophysical Research Letters

RESEARCH LETTER
10.1002/2015GL067370

Key Points:
- MESSENGER data reveal magnetic fields induced at the top of Mercury's core
- The annual induction signal constrains Mercury's core radius to within ±90 km
- Mercury's magnetopause reaches the dayside planetary surface 1.5–4% of the time

Supporting Information:
- Table S1

Correspondence to:
C. L. Johnson,
cjohnson@eos.ubc.ca

Citation:
Johnson, C. L., L. C. Philpott, B. J. Anderson, H. Korth, S. A. Hauck, II, D. Heyner, R. J. Phillips, R. M. Winslow, and S. C. Solomon (2016), MESSENGER observations of induced magnetic fields in Mercury's core, *Geophys. Res. Lett.*, *43*, 2436–2444, doi:10.1002/2015GL067370.

Received 9 DEC 2015
Accepted 29 JAN 2016
Accepted article online 4 FEB 2016
Published online 16 MAR 2016

MESSENGER observations of induced magnetic fields in Mercury's core

Catherine L. Johnson[1,2], Lydia C. Philpott[1], Brian J. Anderson[3], Haje Korth[3], Steven A. Hauck, II[4], Daniel Heyner[5], Roger J. Phillips[6,7], Reka M. Winslow[8], and Sean C. Solomon[9,10]

[1]Department of Earth, Ocean and Atmospheric Sciences, University of British Columbia, Vancouver, British Columbia, Canada, [2]Planetary Science Institute, Tucson, Arizona, USA, [3]The Johns Hopkins University Applied Physics Laboratory, Laurel, Maryland, USA, [4]Department of Earth, Environmental, and Planetary Sciences, Case Western Reserve University, Cleveland, Ohio, USA, [5]Institut für Geophysik und extraterrestrische Physik, Technische Universität Braunschweig, Braunschweig, Germany, [6]Planetary Science Directorate, Southwest Research Institute, Boulder, Colorado, USA, [7]Department of Earth and Planetary Sciences, Washington University in St. Louis, St. Louis, Missouri, USA, [8]Institute for the Study of Earth, Oceans and Space, University of New Hampshire, Durham, New Hampshire, USA, [9]Department of Terrestrial Magnetism, Carnegie Institution of Washington, Washington, District of Columbia, USA, [10]Lamont-Doherty Earth Observatory, Columbia University, Palisades, New York, USA

Abstract Orbital data from the Magnetometer on the MErcury Surface, Space ENvironment, GEochemistry, and Ranging (MESSENGER) spacecraft allow investigation of magnetic fields induced at the top of Mercury's core by time-varying magnetospheric fields. We used 15 Mercury years of observations of the magnetopause position as well as the magnetic field inside the magnetosphere to establish the presence and magnitude of an annual induction signal. Our results indicate an annual change in the internal axial dipole term, g_1^0, of 7.5 to 9.5 nT. For negligible mantle conductivity, the average annual induction signal provides an estimate of Mercury's core radius to within ±90 km, independent of geodetic results. Larger induction signals during extreme events are expected but are challenging to identify because of reconnection-driven erosion. Our results indicate that the magnetopause reaches the dayside planetary surface 1.5–4% of the time.

1. Introduction

Mercury's magnetosphere is distinctive because of the planet's weak magnetic field [*Ness et al.*, 1974, 1975; *Anderson et al.*, 2008, 2011] and proximity to the Sun. Observations by the MErcury Surface, Space ENvironment, GEochemistry, and Ranging (MESSENGER) spacecraft have demonstrated that the long-wavelength global field originates in the core [*Anderson et al.*, 2008; *Uno et al.*, 2009] and is dipolar, axisymmetric, and equatorially asymmetric [*Anderson et al.*, 2011, 2012; *Johnson et al.*, 2012]. The weak internal field and high solar wind dynamic pressure at Mercury lead to a small magnetosphere with an average subsolar distance, R_{SS}, from the dipole origin to the subsolar magnetopause location of ~1.5 R_M [*Winslow et al.*, 2013; *Zhong et al.*, 2015], where $R_M = 2440$ km is Mercury's radius. Temporal variations in solar wind conditions, in particular in the solar wind ram pressure (P_{ram}) and the strength and direction of the interplanetary magnetic field (IMF), together with the short response time of the magnetosphere (the Dungey cycle time), mean that the magnetosphere is also highly dynamic. Aperiodic variations occur frequently with timescales from less than a second to a few minutes [*Anderson et al.*, 2013] and intermittently over several to tens of hours, in particular in association with extreme solar events [*Slavin et al.*, 2009, 2014; *Winslow et al.*, 2015]. However, periodic changes in solar wind pressure occur on Mercury's annual timescale (88 days) as a result of the planet's eccentric orbit.

Temporal variations in P_{ram} can change the position of Mercury's magnetopause. To first order, for a static internal dipole field, $R_{SS} \sim P_{ram}^{-1/6}$ [e.g., *Winslow et al.*, 2013]. The magnetopause is thus expected to approach the planet with increasing P_{ram} and recede from the planet with decreasing P_{ram}. The currents on the magnetopause, and the field generated by them, change accordingly and act to confine the planetary field within the compressed or expanded magnetosphere.

Analyses of MESSENGER gravity data and Earth-based radar measurements of Mercury's rotational state have confirmed the presence of a large metallic core [*Margot et al.*, 2012; *Smith et al.*, 2012; *Hauck et al.*, 2013], which occupies a substantial volume fraction of the magnetosphere. An open question for Mercury has been whether P_{ram}-driven changes in the magnetopause can induce currents at the top of the core that in turn produce

detectable fields at or above the planetary surface [*Hood and Schubert*, 1979; *Suess and Goldstein*, 1979; *Grosser et al*., 2004; *Glassmeier et al*., 2007]. An increase in P_{ram} will compress the magnetosphere and induce currents in the core that increase the planetary field to oppose the decrease in R_{SS}. Conversely, a decrease in P_{ram} leads to a decrease in the planetary field. Induction at Mercury is important for two reasons. First, the induced fields are sensitive to the interior electrical conductivity structure of the planet, which in turn is strongly dependent on the interior temperature distribution. For a simple two-layer electrical conductivity model consisting of an inner conducting sphere and an insulating outer shell, the induced field depends on the geometry and magnitude of the inducing (magnetopause) field and the radius of the conducting sphere, typically interpreted as the radius of the core [*Grosser et al*., 2004; *Glassmeier et al*., 2007]. Second, induction increases the minimum solar wind dynamic pressure needed to compress the dayside magnetosphere to the surface of the planet. This effect, in turn, could substantially inhibit direct bombardment of the dayside surface by the solar wind [*Hood and Schubert*, 1979; *Jia et al*., 2015], with implications for space weathering of the surface and production of exospheric species [e.g., *Leblanc and Johnson*, 2003, 2010; *Wurz et al*., 2010].

Early models of induced fields predicted that, in the absence of reconnection, the dayside surface would be directly exposed to the solar wind ($R_{SS} \sim 1$) for only a small fraction of the time [*Suess and Goldstein*, 1979; *Hood and Schubert*, 1979]. Later studies found similar magnitudes for induced fields [*Grosser et al*., 2004; *Glassmeier et al*., 2007] and predicted that these signals could be detected in observations to be made by the BepiColombo spacecraft [*Grosser et al*., 2004]. The R_{SS}-P_{ram} relationship determined with R_{SS} values inferred from 3 Mercury years of MESSENGER observations, together with ENLIL [*Odstrcil*, 2003] model estimates of P_{ram}, suggested that induction does occur at Mercury [*Winslow et al*., 2013].

This view of compression and expansion of the magnetosphere is complicated by magnetospheric dynamics, driven by magnetopause reconnection and erosion of the dayside magnetospheric field [e.g., *Slavin and Holzer*, 1979]. At Mercury, these dynamics are in turn controlled by the relative orientations and strengths of the IMF and the magnetospheric field at the magnetopause boundary [*Sonnerup*, 1974; *DiBraccio et al*., 2013]. Erosion of dayside flux will act to offset or even exceed the effects of induction, and *Slavin and Holzer* [1979] concluded that this effect could reduce R_{SS} by 0.2 R_M to 0.7 R_M from its uneroded value up to 60% of the time. MESSENGER observations of the reconnection rate across the magnetopause [*DiBraccio et al*., 2013] and of three extreme solar wind events [*Slavin et al*., 2014] support this notion and indicate that, at least under extreme conditions, the effects of induction are secondary to those of reconnection-driven erosion.

MESSENGER Magnetometer (MAG) data taken in orbit around Mercury from 23 March 2011 to 30 April 2015 allow a systematic investigation of induction. We focus on the annual signal for several reasons. First, because P_{ram} varies as r_h^{-2}, where r_h is heliocentric distance, the R_{SS}-P_{ram} relationship can be recast in terms of heliocentric distance, removing the need for independent estimates of P_{ram} that were not routinely available from the suite of plasma sensors on MESSENGER. Second, the multiple Mercury years of MESSENGER orbital observations allow robust detection of an annual signal using only magnetospherically quiet orbits [*Anderson et al*., 2013]. Third, periodic forcing on this 88 day timescale allows us to apply the two-layer electrical conductivity model of *Grosser et al*. [2004]. The model formulation and the observed annual signal constrain the radius of the top of the highly electrically conductive region, providing an assessment of Mercury's core radius that is independent of traditional geodetic approaches [*Hauck et al*., 2013].

2. MESSENGER Observational Constraints on Induced Core Fields

Induced fields, if sufficiently large, will have two observable effects that can be investigated with MESSENGER MAG data. In the absence of induction, R_{SS} will vary as $r_h^{1/3}$. If induction occurs, the induced fields effectively dampen the compression and expansion of the magnetosphere driven by variations in solar wind density (and hence P_{ram}) with heliocentric distance. As a result, R_{SS} will vary as r_h^b, where the exponent b is less than 1/3. In addition, the change in the planetary field due to induction can be investigated using observations inside the magnetosphere. The largest induction signals will be in the axial dipole term, g_1^0, in the internal field (see section 3): a relative increase in the dipole moment will occur at perihelion, and a decrease will occur at aphelion. We examined these effects with 15 Mercury years of MESSENGER MAG data taken in orbit around Mercury.

MESSENGER observed both the planetary and the interplanetary magnetic fields on every orbit, and the magnetopause boundary locations are readily identified in the data. Data were analyzed in Mercury solar orbital

(MSO) coordinates, for which +*X* is sunward, +*Z* is northward, and +*Y* completes the right-handed system. MSO positions at the magnetopause and inside the magnetosphere were corrected for solar wind aberration using Mercury's instantaneous orbital speed, an average solar wind speed of 402 km/s [cf. *Johnson et al.*, 2012], and the dipole offset [*Anderson et al.*, 2013].

2.1. Magnetopause Position: Variation With Heliocentric Distance

We identified magnetopause crossings on the inbound and outbound segments of MESSENGER orbits from 24 March 2011 through 31 October 2014 using the approach of *Winslow et al.* [2013] and calculated the magnetic disturbance index [*Anderson et al.*, 2013] for each orbit. The average magnetopause position was computed for each inbound or outbound orbit segment from the inner and outer limits to the magnetopause crossings (supporting information Table S1). Magnetopause positions near perihelion were observed to be systematically closer to the planet than those at aphelion. For each magnetopause position, we computed R_{SS} with the *Shue et al.* [1997] functional form for magnetopause shape, under rotational symmetry and with an average flaring parameter, $\alpha = 0.5$. α governs whether the magnetotail is closed ($\alpha < 0.5$) or open ($\alpha \geq 0.5$), and we confirmed that the best fit value of 0.5 found by *Winslow et al.* [2013] is appropriate for our larger data set of magnetopause crossings. The R_{SS} values were computed for magnetopause crossings sunward of $X = -2\,R_M$ to minimize sensitivity to variations in tail flaring. More magnetopause crossings are observed near aphelion and perihelion than at the average r_h, reflecting the variation in Mercury orbital angular velocity with r_h. R_{SS} values increase on average with increasing r_h, but there is considerable scatter at any given r_h. In general, lower R_{SS} values are seen on orbits with greater magnetospheric activity. The activity index is a measure of relative magnetic variability for each orbit at periods of 0.1 s to 300 s [*Anderson et al.*, 2013]. The physical processes contributing to the activity index include signatures of magnetospheric dynamics associated with reconnection and erosion, which can modify or mask any induction signals. We therefore restricted our investigations of an annual induction signal to magnetically quiet orbits.

We selected orbits with an activity index less than 33, i.e., the quietest one-third of the data. The activity index is normalized for local time, such that the distribution of heliocentric distance for the 1943 quiet crossings mirrors that of the full data set. The magnetopause crossings were considered to be statistically independent given that timescales for magnetospheric variability are much less than the time interval between successive crossings. We investigated a least-squares fit, $R_{SS} = a\ r_h^b$, and computed the 95% confidence limits on b (reported as $\pm\ \Delta b$). We found an exponent $b = 0.29 \pm 0.03$ (Figure 1b). Thus, at the 95% confidence level the value for b is significantly different from the value of 1/3 expected in the absence of induction. The fit results were insensitive to the quiet-orbit selection criteria: $b = 0.28 \pm 0.04$ (880 orbits) for an activity index cutoff of 15 and $b = 0.29 \pm 0.02$ (2362 orbits) for a cutoff of 40. The R_{SS}-P_{ram} relationship found by *Winslow et al.* [2013] can be related to an R_{SS}-r_h relationship, under the assumption that the P_{ram} variations in the ENLIL model used by *Winslow et al.* [2013] reflect mainly r_h variations. The resulting value of b is 0.296, in excellent agreement with that found here. However, the smaller data set (and lack of restriction to quiet orbits) yielded 95% confidence limits of $b = 0.248$–0.344 and could not confirm that the value was statistically different from $b = 0.33$ (no induction).

If the induced field signature at the magnetopause boundary is dominantly dipolar in geometry, the R_{SS}-r_h relationship can be related to the induced dipole moment. Between aphelion ($r_h = r_a$) and perihelion ($r_h = r_p$), the change in dipole moment, f, expressed as a fraction of the dipole moment in the absence of induction is given by $f = (r_p/r_a)^{3b-1} - 1$. Our value for b corresponds to a 5% change in dipole moment, with lower and upper 95% confidence limits of 2% and 8%. For a mean dipole moment of 190 nT R_M [*Johnson et al.*, 2012; *Korth et al.*, 2015], this change in dipole moment is 9.5 nT R_M, with 95% confidence limits of 3.8–15.2 nT $R_M{}^3$.

2.2. Field Inside the Magnetosphere: Aphelion Versus Perihelion

We selected two subsets of quiet orbits to investigate changes in the field measured inside the magnetosphere within 0.005 AU of perihelion (76 orbits) and 0.002 AU of aphelion (93 orbits). We used the KT14 magnetospheric model [*Korth et al.*, 2015] and the approach of *Johnson et al.* [2012] to find the best fit dipole moment (m) for each subset. The KT14 tail field parameters, dipole offset, and dipole tilt (zero) were as specified by *Korth et al.* [2015], and the R_{SS} values were set to the mean values computed from the subsets of perihelion and aphelion orbit subsets (1.4 R_M and 1.6 R_M, respectively). For each R_{SS}-m model-parameter pair, the model shielding fields were recomputed. The root-mean-square (RMS) misfit of the resulting model field to the observations

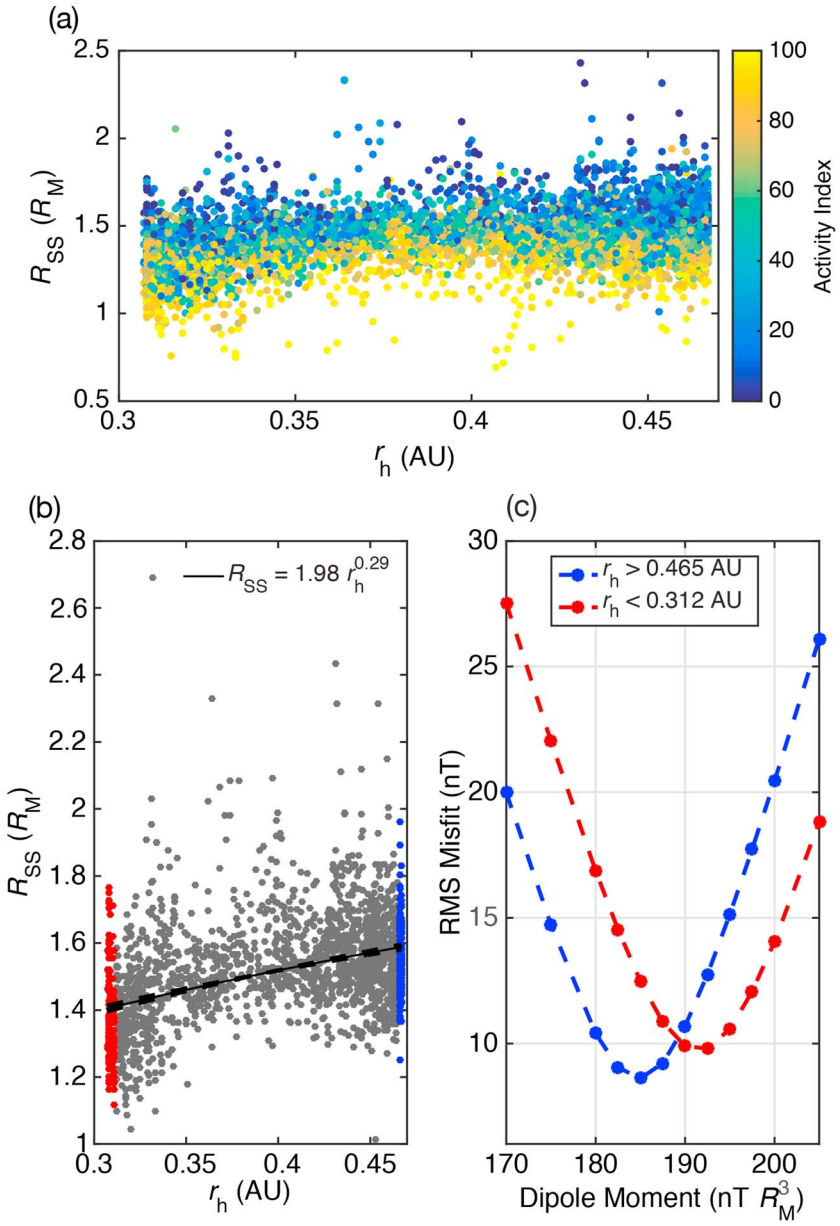

Figure 1. (a) Subsolar distance, R_{SS}, versus heliocentric distance, r_h, computed for magnetopause crossings spanning the period 24 March 2011 to 31 October 2014 (15 Mercury years) for which $X_{MSO} > -2\,R_M$ and color coded by activity index. One crossing for which $R_{SS} > 2.5\,R_M$ is not shown. (b) R_{SS} versus r_h for 1943 quiet orbits (see text) along with the best-fit power law $R_{SS} = 1.98\,r_h^{0.29}$ (black solid line) and 95% confidence limits (black dashed lines). Red and blue dots denote R_{SS} values for 76 and 93 orbits within 0.005 AU of perihelion and 0.002 AU of aphelion, respectively. (c) RMS misfit of predicted B_r to observed B_r inside the magnetosphere as a function of dipole moment for orbits near perihelion (red) and aphelion (blue).

was calculated using only the radial component of the magnetic field, in order to minimize the effects of residual contributions on the horizontal field components from field-aligned currents [*Anderson et al.*, 2014] observed in MESSENGER's dawn-dusk orbit geometry near perihelion and aphelion. The dipole moment was varied in steps of 5 nT R_M initially and then in steps of 2.5 nT R_M^3 near the minima in RMS misfit.

The RMS misfit curves (Figure 1c) are systematically offset from each other, with the best-fit dipole moment at aphelion 7.5 nT R_M greater than that at perihelion, consistent with the presence of an induction signal and in good agreement with the mean change in dipole moment inferred from the R_{SS}-r_h relationship. Formal 95% confidence limits for the best-fit dipole moment derived from the number of magnetic field measurements in

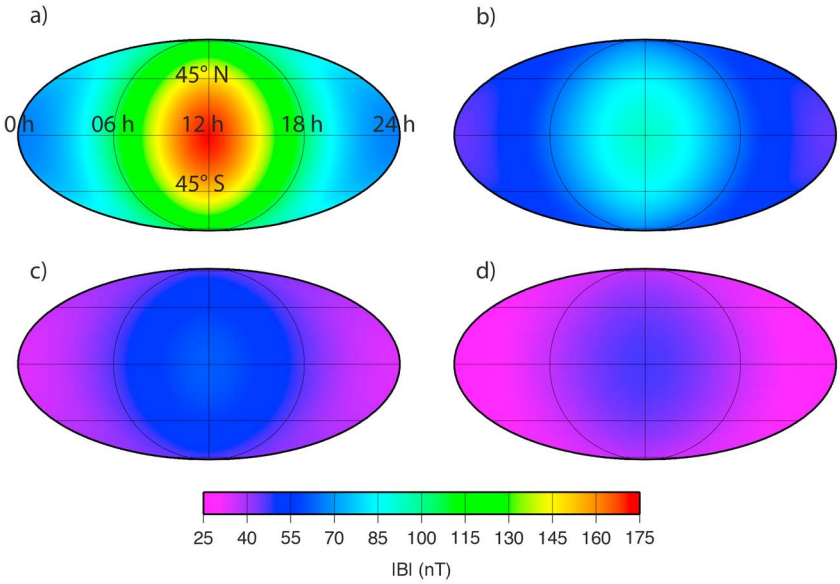

Figure 2. Strength of the model magnetopause field at Mercury's core-mantle boundary (radius, $R_C = 2020$ km [*Hauck et al.*, 2013]) for (a) $R_{SS} = 1.15\,R_M$, (b) $R_{SS} = 1.40\,R_M$, (c) $R_{SS} = 1.60\,R_M$, and (d) $R_{SS} = 1.75\,R_M$. The field strength is computed with the KT14 magnetospheric model [*Korth et al.*, 2015]. The same color scale is used throughout to emphasize the change in the field strength across the four cases. Grid lines are spaced at 45° in latitude and 6 h in local time, and each plot is centered on noon at the equator. The large-scale day/night and latitudinal variations in the field are most easily seen in Figure 2a.

each subset correspond to an increase in RMS misfit above the minimum RMS of only ~0.2 nT. We regard this figure as unrealistically small, so we do not quote these uncertainties here.

3. Predicted Induction Signatures

We adopted the two-layer electrical conductivity model of *Grosser et al.* [2004], which includes an inner conducting sphere, of conductivity σ_0 (~10^6 S/m) and radius R_{COND}, and an insulating silicate shell ($\sigma_m \sim 0$). For silicate conductivities similar to those of terrestrial mantle materials [*Constable*, 1993] and proposed for Mercury [*Verhoeven et al.*, 2009], the characteristic time for external field variations to diffuse from the surface to the core is O(1 h). For longer periods and a sufficiently high conductivity contrast (σ_0-σ_m), induction in the mantle and crust is negligible relative to that in the core. Under these assumptions, the transfer function between the induced and the inducing fields at a given period is

$$\frac{I_n^m}{E_n^m} = \frac{n}{n+1} q^{2n+1} \tag{1}$$

where I_n^m and E_n^m are coefficient pairs [g_n^m, h_n^m] and [G_n^m, H_n^m], which are the induced and inducing spherical harmonic Gauss coefficients of degree n and order m in the planetocentric local time frame, for the internal and external fields, respectively [*Olsen et al.*, 2010], and $q = R_{COND}/R_M$ [*Rikitake*, 1966; *Grosser et al.*, 2004]. (Note that the external field coefficients are typically given by [q_n^m, s_n^m] in the geomagnetic literature). Typically, R_{COND} is assumed to be the radius of the core, R_C. Prior to the MESSENGER mission, R_C was constrained by the Mariner 10 estimate of Mercury's mass and possible interior composition models. A commonly used value for R_C was 1800 km, with a permitted range from ~1760 km to 2200 km [*Harder and Schubert*, 2001; *Hauck et al.*, 2007] and even to 2400 km [*Harder and Schubert*, 2001]. MESSENGER observations of Mercury's gravity field, in combination with Earth-based observations of Mercury's rotational state, have enabled the radius of Mercury's liquid outer core to be well determined at $R_C = 2020 \pm 30$ km [*Hauck et al.*, 2013]. Furthermore, the possibility of a solid FeS layer at the base of the silicate mantle has been proposed [*Hauck et al.*, 2013], although experimental work relating Mercury's core composition to MESSENGER's observations of surface composition suggest that the conditions under which such a layer could occur are highly restrictive [*Chabot et al.*, 2014]. If present, such a layer may have an electrical conductivity much

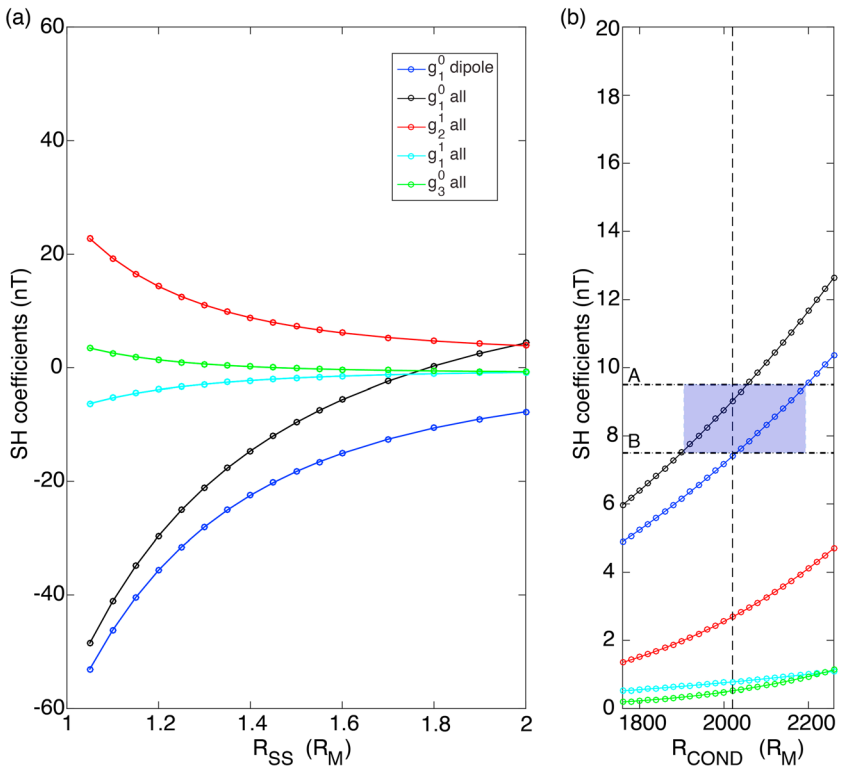

Figure 3. (a) Induced spherical harmonic (SH) terms g_1^0, g_2^1, g_1^1, and g_3^0 versus subsolar distance, R_{SS}. Coefficients are computed from the full external field (the tail field and both the dipole and tail shielding fields) from the KT14 model [*Korth et al.*, 2015] for R_{COND} = 2020 km [*Hauck et al.*, 2013]. The induced g_1^0 term for a magnetopause field that shields only the planetary dipole field is also shown. (b) The predicted annual induction signal resulting from a change in R_{SS} from 1.4 R_M to 1.6 R_M as a function of R_{COND}. The dashed vertical line denotes R_{COND} = 2020 km. Dotted horizontal lines are the mean values for the annual g_1^0 induction signal inferred from R_{SS}-r_h (labeled "A") and the field inside the magnetosphere (labeled "B"). The shaded region indicates the range of R_{COND} consistent with the observed average dipole induction signal and the predicted values from the KT14 model.

greater than that of the silicate rocks above it; under such a scenario, R_{COND} would reflect the radius of the top of this layer rather than R_C.

The inducing field geometry was obtained by a spherical harmonic expansion of the KT14 magnetopause fields in the MSO frame. Because the KT14 model describes only a static magnetosphere, we represented the temporally varying magnetopause field by a series of quasi-static states and computed the spherical harmonic expansion of the magnetopause field at distinct R_{SS} values from R_{SS} = 1.05 R_M to 2.0 R_M. The lower limit of R_{SS} = 1.05 R_M is set by the R_{SS} value for which the magnetopause first touches the surface of the planet in the southern hemisphere owing to the equatorial asymmetry in the internal field. Changes in R_{SS} result in substantial changes in magnetopause field strength at the core-mantle boundary (CMB) (Figure 2). For example, the maximum dayside magnetopause field strengths at the CMB are 171 nT for R_{SS} = 1.15 R_M and 47 nT for R_{SS} = 1.75 R_M. For the annual average variation in R_{SS} the maximum magnetopause field strength at the CMB varies from 62 to 92 nT. The inducing field is dominated by the G_1^0 and G_2^1 terms, reflecting the equator-to-pole and day-night structure in the magnetopause field, respectively.

The transfer function in equation (1) predicts that the ratios of the magnitudes of the induced to inducing fields are 28%, 26%, and 20% for spherical harmonic degrees 1, 2, and 3, respectively. The resulting largest induced terms (g_1^0, g_2^1, g_1^1, and g_3^0) are shown for the quasi-static states in Figure 3a. The actual induction signals resulting from a change in R_{SS} and the predicted values are shown in Figure 3b for the pre-MESSENGER range of R_{COND}. The magnetopause fields shield both the planetary field and the fields from current systems inside the magnetosphere, notably the field resulting from the tail current sheet. The geometry of the tail current sheet, particularly its proximity to the planet on the nightside, is less well constrained by MESSENGER

data than the magnetopause geometry. We estimated the effects of the uncertainty in our knowledge of the tail field on the resulting shielding field by computing the induced g_1^0 term resulting from (a) a magnetopause field that shields only the planetary dipole field and (b) the full external field, including the tail field and magnetopause fields that shield both the dipole and the tail field (Figure 3). The corresponding predicted g_1^0 induction signals for $R_{COND} = 2020$ km are 7.5 and 9.0 nT (Figure 3b).

4. Discussion and Conclusions

MESSENGER observations of Mercury's magnetopause position and of the field inside the magnetosphere show evidence for an annual induction signal. The inferred average changes in the axial dipole term from the two distinct approaches are 7.5 and 9.5 nT. The 95% confidence limits on the induced dipole term obtained from the R_{SS}-r_h relationship are relatively large (4–15 nT) but confirm that the induction signal is distinct from zero. The average values obtained from the two approaches show excellent agreement with the predicted values for $R_{COND} = R_C = 2020$ km [*Hauck et al*., 2013], given uncertainties in the tail field (Figure 3b).

The observed average annual induction signal obtained from two distinct methods constrains R_{COND} to within 160–180 km for a given external field model and under the assumption of negligible mantle conductivity (Figure 3b). The predicted induced signal for the full external field indicates that $R_{COND} = 1900$–2060 km is compatible with the signal inferred from observations. For an external field corresponding to only the dipole shielding field, a larger conductive radius is required to match the observed signal ($R_{COND} = 2020$–2200 km). Importantly, pre-MESSENGER canonical values for MESSENGER's core radius (~1800 km) are not favored by the observed average signal.

The approach taken here to modeling induced fields differs from the orbit-by-orbit approach typically used at Earth [e.g., *Hulot et al*., 2015; *Sabaka et al*., 2015] because of the still-limited characterization of Mercury's external fields and the limited spatial coverage of MESSENGER's highly eccentric orbit. For example, efforts underway to characterize the dependence of the large-scale magnetospheric fields on activity [*Anderson et al*., 2013] and to incorporate field-aligned currents [*Anderson et al*., 2014] are important to future work. Refinement of the estimate of R_{COND} and interior conductivity structure more generally requires improved knowledge of the inducing field geometry and information at periods other than 1 year.

A related open question is whether time variations in Mercury's internal magnetic field could result from librationally driven core flow. Although this process would not predict the correspondence of internal and external field variations observed here, it is still of interest to examine. The magnetic Reynolds number associated with the forced libration is O(1), suggesting that such a mechanism is only marginally possible. Full treatment of this issue would require detailed assessment of possible driving instabilities [e.g., *LeBars et al*., 2015] and the resulting poloidal (observable) field.

Larger changes in P_{ram} (and hence in R_{SS}) will yield a larger induction signal, and the contributions to the induced fields from spherical harmonic terms beyond g_1^0, notably g_2^1, might be detectable. We examined the entire MESSENGER data set for orbit-to-orbit changes in the peak field strength and in R_{SS} to assess whether there were any candidate orbits with obvious large induction signals. We defined the average peak field strength, B_P, to be the average of the peak field strength measured on three orbits preceding, and three orbits following, a given orbit. The change in peak field strength ΔB_P was then defined to be the difference between the peak field strength on that orbit and B_P. We found 14 orbits with ΔB_P greater than 10% (i.e., approximately twice the equivalent annual induction signal amplitude). Of these orbits, 12 occurred at times of extreme events [e.g., *Winslow et al*., 2015], and the remaining two had activity indices of 97.6 and 98.8, corresponding to highly disturbed conditions. Extreme events are difficult to model from an induction perspective with MESSENGER data, not only because of the additional effect of reconnection-driven erosion but because both the tail field and magnetopause geometry are highly time dependent. MESSENGER's orbit combined with this time dependence implies that knowledge of the inducing field is poor on these timescales. Figure 3 shows that even for a given magnetopause geometry, uncertainties in the tail field are important and translate directly into uncertainties in the inferred interior electrical conductivity structure. The upcoming BepiColombo mission will offer substantive advances to induction studies because the plasma ram and thermal pressures will be measured, magnetic field observations will be obtained from two spacecraft simultaneously, and improved coverage of the magnetotail will be obtained [*Glassmeier et al*., 2010].

Our observations of Mercury's magnetopause position allow quantification of the percentage of the time that the magnetopause reaches the planetary surface. For a magnetopause shape with $\alpha = 0.5$, this situation occurs when R_{SS} is less than 1.05 R_M. For a more flared magnetopause, the critical R_{SS} value decreases, and vice versa; e.g., for $\alpha = 0.4$ to 0.6 the critical value of R_{SS} ranges from 1.06 R_M to 1.04 R_M. From our average magnetopause crossings and the corresponding magnetopause shape, we find R_{SS} to be less than 1.05 R_M on 1.5% of the observed magnetopause transits. Innermost limits on the magnetopause crossings yield R_{SS} values less than 1.05 R_M on 4% of the crossings. We infer that at least some of the dayside is directly exposed to the solar wind between 1.5% and 4% of the time. Although this percentage is small, when integrated over time it suggests that intermittent direct bombardment of the dayside, in addition to the quasi-steady bombardment observed in the cusp [*Raines et al*., 2014, 2015; *Winslow et al*., 2014; *Gershman et al*., 2015], plays an important role in space weathering the surface and in the generation of the exosphere.

Acknowledgments
The MESSENGER mission is supported by the NASA Discovery Program, under contracts NAS5-97271 to The Johns Hopkins University Applied Physics Laboratory and NASW-00002 to the Carnegie Institution of Washington, as well as the MESSENGER Participating Scientist Program. C.L.J. and L.C.P. also acknowledge support from the Natural Sciences and Engineering Research Council of Canada. Daniel Heyner was supported by the German Ministerium für Wirtschaft und Energie and the German Zentrum für Luft- und Raumfahrt under contract 50 QW 1501. All MESSENGER data analyzed for this paper are publicly available at the NASA Planetary Data System. We thank Richard Holme and David Stevenson for constructive reviews.

References

Anderson, B. J., M. H. Acuña, H. Korth, M. E. Purucker, C. L. Johnson, J. A. Slavin, S. C. Solomon, and R. L. McNutt Jr. (2008), The structure of Mercury's magnetic field from MESSENGER's first flyby, *Science*, *321*, 82–85.

Anderson, B. J., C. L. Johnson, H. Korth, M. E. Purucker, R. M. Winslow, J. A. Slavin, S. C. Solomon, R. L. McNutt Jr., J. M. Raines, and T. H. Zurbuchen (2011), The global magnetic field of Mercury from MESSENGER orbital observations, *Science*, *333*, 1859–1862, doi:10.1126/science.1211001.

Anderson, B. J., C. L. Johnson, H. Korth, R. M. Winslow, J. E. Borovsky, M. E. Purucker, J. A. Slavin, S. C. Solomon, M. T. Zuber, and R. L. McNutt Jr. (2012), Low-degree structure in Mercury's planetary magnetic field, *J. Geophys. Res.*, *117*, E00L12, doi:10.1029/2012JE004159.

Anderson, B. J., C. L. Johnson, and H. Korth (2013), A magnetic disturbance index for Mercury's magnetic field derived from MESSENGER Magnetometer data, *Geochem. Geophys. Geosyst.*, *14*, 3875–3886, doi:10.1002/ggge.20242.

Anderson, B. J., C. L. Johnson, H. Korth, J. A. Slavin, R. M. Winslow, R. J. Phillips, R. L. McNutt Jr., and S. C. Solomon (2014), Steady-state field-aligned currents at Mercury, *Geophys. Res. Lett.*, *41*, 7444–7452, doi:10.1002/2014GL061677.

Chabot, N. L., E. A. Wollack, R. L. Klima, and M. E. Minitti (2014), Experimental constraints on Mercury's core composition, *Earth Planet. Sci. Lett.*, *390*, 199–208, doi:10.1016/j.epsl.2014.01.004.

Constable, S. (1993), Constraints on mantle electrical conductivity from field and laboratory measurements, *J. Geomag. Geoelectr.*, *45*, 707–728.

DiBraccio, G. A., J. A. Slavin, S. A. Boardsen, B. J. Anderson, H. Korth, T. H. Zurbuchen, J. M. Raines, D. N. Baker, R. L. McNutt Jr., and S. C. Solomon (2013), MESSENGER observations of magnetopause structure and dynamics at Mercury, *J. Geophys. Res. Space Physics*, *118*, 997–1008, doi:10.1002/jgra.50123.

Gershman, D. J., et al. (2015), MESSENGER observations of solar energetic electrons within Mercury's magnetosphere, *J. Geophys. Res. Space Physics*, *120*, 8559–8571, doi:10.1002/2015JA021610.

Glassmeier, K.-H., J. Grosser, U. Auster, D. Constantinescu, Y. Narita, and S. Stellmach (2007), Electromagnetic induction effects and dynamo action in the Hermean system, *Space Sci. Rev.*, *132*, 511–527.

Glassmeier, K.-H., et al. (2010), The fluxgate magnetometer of the BepiColombo Mercury Planetary Orbiter, *Planet. Space Sci.*, *58*, 287–299, doi:10.1016/j.pss.2008.06.018.

Grosser, J., K.-H. Glassmeier, and A. Stadelmann (2004), Induced magnetic field effects at planet Mercury, *Planet. Space Sci.*, *52*, 1251–1260.

Harder, H., and G. Schubert (2001), Sulfur in Mercury's core?, *Icarus*, *151*, 118–122.

Hauck, S. A., II, S. C. Solomon, and D. A. Smith (2007), Predicted recovery of Mercury's internal structure by MESSENGER, *Geophys. Res. Lett.*, *34*, L18201, doi:10.1029/2007GL030793.

Hauck, S. A., II, et al. (2013), The curious case of Mercury's internal structure, *J. Geophys. Res. Planets*, *118*, 1204–1220, doi:10.1002/jgre.20091.

Hood, L. L., and G. Schubert (1979), Inhibition of solar wind impingement on Mercury by planetary induction currents, *J. Geophys. Res.*, *84*, 2641–2647.

Hulot, G., T. J. Sabaka, N. Olsen, and A. Fournier (2015), The present and future geomagnetic field, in *Geomagnetism*, edited by M. Kono, *Treatise on Geophysics*, 2nd ed., edited by G. Schubert, vol. 5, pp. 33–78, Elsevier, Amsterdam, Netherlands.

Jia, X., J. A. Slavin, T. I. Gombosi, L. K. S. Daldorff, G. Toth, and B. van der Holst (2015), Global MHD simulations of Mercury's magnetosphere with coupled planetary interior: Induction effect of the planetary conducting core on the global interaction, *J. Geophys. Res. Space Physics*, *120*, 4763–4775, doi:10.1002/2015JA021143.

Johnson, C. L., et al. (2012), MESSENGER observations of Mercury's magnetic field structure, *J. Geophys. Res.*, *117*, E00L14, doi:10.1029/2012JE004217.

Korth, H., N. A. Tsyganenko, C. L. Johnson, L. C. Philpott, B. J. Anderson, M. M. Al Asad, S. C. Solomon, and R. L. McNutt Jr. (2015), Modular model for Mercury's magnetospheric magnetic field confined within the average observed magnetopause, *J. Geophys. Res. Space Physics*, *120*, 4503–4518, doi:10.1002/2015JA021022.

LeBars, M., D. Cébron, and P. Le Gal (2015), Flows driven by libration, precession and tides, *Annu. Rev. Fluid Mech.*, *47*, 163–193.

Leblanc, F., and R. E. Johnson (2003), Mercury's sodium exosphere, *Icarus*, *164*, 261–281.

Leblanc, F., and R. E. Johnson (2010), Mercury exosphere, I. Global circulation model of its sodium component, *Icarus*, *209*, 280–300.

Margot, J. L., S. J. Peale, S. C. Solomon, S. A. Hauck II, F. D. Ghigo, R. F. Jurgens, M. Yseboodt, J. D. Giorgini, S. Padovan, and D. B. Campbell (2012), Mercury's moment of inertia from spin and gravity data, *J. Geophys. Res.*, *117*, E00L09, doi:10.1029/2012JE004161.

Ness, N. F., K. W. Behannon, R. P. Lepping, Y. C. Whang, and K. H. Schatten (1974), Magnetic field observations near Mercury: Preliminary results from Mariner 10, *Science*, *185*, 151–160, doi:10.1126/science.185.4146.151.

Ness, N. F., K. W. Behannon, R. P. Lepping, and Y. C. Whang (1975), Magnetic field of Mercury confirmed, *Nature*, *255*, 204–205, doi:10.1038/255204a0.

Odstrcil, D. (2003), Modeling 3-D solar wind structure, *Adv. Space Res.*, *32*, 497–506, doi:10.1016/S0273-1177(03)00332-6.

Olsen, N., K.-H. Glassmeier, and X. Jia (2010), Separation of the magnetic field into external and internal parts, *Space Sci. Rev.*, *152*, 135–157.

Raines, J. M., D. J. Gershman, J. A. Slavin, T. H. Zurbuchen, H. Korth, B. J. Anderson, and S. C. Solomon (2014), Structure and dynamics of Mercury's magnetospheric cusp: MESSENGER measurements of protons and planetary ions, *J. Geophys. Res. Space Physics*, *119*, 6587–6602, doi:10.1002/2014JA020120.

Raines, J. M., et al. (2015), Plasma sources in planetary magnetospheres: Mercury, *Space Sci. Rev.*, *192*, 91–144, doi:10.1007/s11214-015-0193-4.
Rikitake, T. (1966), *Electromagnetism and the Earth's Interior, Developments in Solid Earth Geophysics*, vol. 2, Elsevier, Amsterdam, Netherlands.
Sabaka, T. J., N. Olsen, R. H. Tyler, and A. Kuvshinov (2015), CM5, a pre-*Swarm* comprehensive geomagnetic field model derived from over 12 yr of CHAMP, Ørsted, SAC-C and observatory data, *Geophys. J. Int.*, *200*, 1596–1626.
Shue, J.-H., J. K. Chao, H. C. Fu, C. T. Russell, P. Song, K. K. Khurana, and H. J. Singer (1997), A new functional form to study the solar wind control of the magnetopause size and shape, *J. Geophys. Res.*, *102*, 9497–9511.
Slavin, J. A., and R. E. Holzer (1979), The effect of erosion on the solar wind stand-off distance at Mercury, *J. Geophys. Res.*, *84*, 2076–2082.
Slavin, J. A., et al. (2009), MESSENGER observations of magnetic reconnection in Mercury's magnetosphere, *Science*, *324*, 606–610.
Slavin, J. A., et al. (2014), MESSENGER observations of Mercury's dayside magnetosphere under extreme solar wind conditions, *J. Geophys. Res. Space Physics*, *119*, 8087–8116, doi:10.1002/2014JA020319.
Smith, D. E., et al. (2012), Gravity field and internal structure of Mercury from MESSENGER, *Science*, *336*, 214–217, doi:10.1126/science.1218809.
Sonnerup, B. U. Ö. (1974), Magnetopause reconnection rate, *J. Geophys. Res.*, *79*, 1546–1549.
Suess, S. T., and B. E. Goldstein (1979), Compression of the Hermean magnetosphere by the solar wind, *J. Geophys. Res.*, *84*, 3306–3312.
Uno, H., C. L. Johnson, B. J. Anderson, H. Korth, and S. C. Solomon (2009), Modeling Mercury's internal magnetic field with smooth inversions, *Earth Planet. Sci. Lett.*, *285*, 328–339.
Verhoeven, O., P. Tarits, P. Vacher, A. Rivoldini, and T. Van Hoolst (2009), Composition and formation of Mercury: Constraints from future electrical conductivity measurements, *Planet. Space Sci.*, *57*, 296–305.
Winslow, R. M., B. J. Anderson, C. L. Johnson, J. A. Slavin, H. Korth, M. E. Purucker, D. N. Baker, and S. C. Solomon (2013), Mercury's magnetopause and bow shock from MESSENGER Magnetometer observations, *J. Geophys. Res. Space Physics*, *118*, 2213–2227, doi:10.1002/jgra.50237.
Winslow, R. M., et al. (2014), Mercury's surface magnetic field determined from proton-reflection magnetometry, *Geophys. Res. Lett.*, *41*, 4463–4470, doi:10.1002/2014GL060258.
Winslow, R. M., N. Lugaz, L. C. Philpott, N. A. Schwadron, C. J. Farrugia, B. J. Anderson, and C. W. Smith (2015), Interplanetary coronal mass ejections from MESSENGER orbital observations at Mercury, *J. Geophys. Res. Space Physics*, *120*, 6101–6118, doi:10.1002/2015JA021200.
Wurz, P., J. A. Whitby, U. Rohner, J. A. Martín-Fernández, H. Lammer, and C. Kolb (2010), Self-consistent modelling of Mercury's exosphere by sputtering, micro-meteorite impact and photon-stimulated desorption, *Planet. Space Sci.*, *58*, 1599–1616.
Zhong, J., W. X. Wan, J. A. Slavin, Y. Wei, R. L. Lin, L. H. Chai, J. M. Raines, Z. J. Rong, and X. H. Han (2015), Mercury's three-dimensional asymmetric magnetopause, *J. Geophys. Res. Space Physics*, *120*, 7658–7671, doi:10.1002/2015JA021425.